

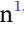









RESEARCH ARTICLE OPEN ACCESS

Device Simulation Analysis of the Perovskite/Perovskite/Silicon Triple Junction Solar Cell Structure

Luis Restat^{1,2}  | Christoph A. Messmer^{1,2}  | Jonas Schön^{1,2}  | Minasadat Heydarian^{1,2}  | Maryamsadat Heydarian^{1,2}  | Patricia S. C. Schulze¹  | Kerem Artuk³  | Christian M. Wolff³  | Andreas Fell¹  | Schubert¹ | Stefan Glunz^{1,2} 

¹Fraunhofer Institute for Solar Energy Systems ISE, Freiburg, Germany | ²Chair for Photovoltaic Energy Conversion, Department of Sustainable Systems Engineering (INATECH), University of Freiburg, Freiburg, Germany | ³École Polytechnique Fédérale de Lausanne (EPFL), Institute of Electrical and Microengineering (IEM), Photovoltaics and Thin-Film Electronics Laboratory (PV-Lab), Neuchâtel, Switzerland

Correspondence: Luis Restat (luis.restat@ise.fraunhofer.de)

Received: 20 October 2025 | **Revised:** 5 December 2025 | **Accepted:** 15 December 2025

Keywords: perovskite/perovskite/silicon solar cells | photovoltaics | sentaurus technology computer-aided design | simulation

ABSTRACT

In recent years, the development of perovskite/perovskite/silicon triple junction solar cells has received considerable attention, aiming to exceed the efficiency of perovskite/silicon dual junction solar cells. Various challenges must be addressed to reach these efficiencies and justify the additional complexity. This article outlines a simulation-based roadmap for improving the structure of these cells. It discusses critical issues and estimates potential improvements for perovskite/perovskite/silicon solar cells based on device architectures developed at Fraunhofer ISE and EPFL. The article describes potential challenges related to thickening the middle perovskite absorber to achieve current matching. It explains the observed losses in fill factor in the top cell with a high bandgap, which arise from an insufficient hole barrier caused by unfavorable valence-band alignment between the perovskite and the electron transport layer. These aspects are examined through numerical device simulations.

1 | Introduction

In the field of perovskite multijunction solar cells, perovskite/perovskite/silicon triple junction solar cells have attracted growing interest in recent years. From the first proof of concept in 2018 [1], several improvements have been made on this structure [2]. Perovskite compositions have become more stable and less prone to nonradiative recombination [3–9]. Deposition techniques [6, 10, 11], suitable charge transport layers [7, 12], and interface passivation [5, 7, 13] have been engineered, light management has been improved [3, 10, 11, 14], and appropriate characterization techniques have been developed [5, 10]. These advances led to a significant increase in efficiency up to 30.5% [15]. However, to justify the increased complexity that comes with a triple junction compared to the perovskite/silicon tandem, the efficiency of the triple junction must eventually exceed that of the dual junction devices, which currently have a record of 34.85% [16].

To illustrate the current state of the triple junction, Figure 1 shows an overview of different efficiency limits of silicon-based single, dual and triple cell structures. In previous publications, we assigned a “practical potential” to the perovskite/silicon dual junction [19] and the perovskite/perovskite/silicon solar cells [20] based on a detailed opto-electrical device simulation. In terms of optics, the bandgaps and thicknesses of the absorbers are chosen to achieve balanced absorption, while the interlayers are kept as thin as possible to minimize parasitic absorption. The maximum thickness of the perovskite absorbers is set to 1500 nm to reflect the latest advancements. The electrical simulation is conducted with idealized electrical parameters, i.e., high charge carrier lifetimes, no nonradiative recombination, perfect band alignments for the transport layers, and no ionic effects or series resistances. The efficiency gap between the current experimental record and the practical potential efficiency is much smaller for the dual junction structure than for the triple structure. From the current triple junction cell efficiency record (experimental) of

This is an open access article under the terms of the [Creative Commons Attribution](https://creativecommons.org/licenses/by/4.0/) License, which permits use, distribution and reproduction in any medium, provided the original work is properly cited.

© 2026 The Author(s). *Solar RRL* published by Wiley-VCH GmbH.

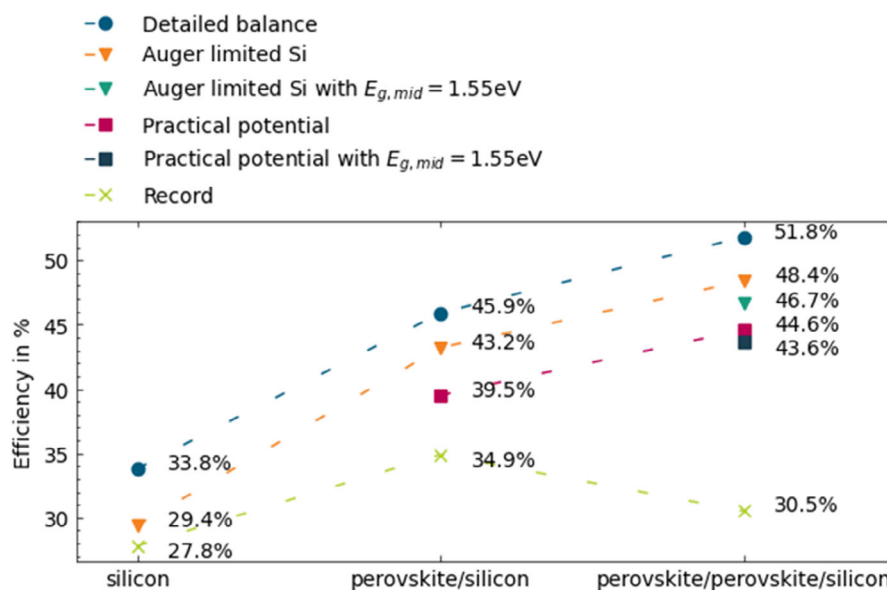


FIGURE 1 | Overview of the theoretical efficiencies for single, dual junction and triple junction solar cells. The different scenarios are the detailed balance limit [17], Auger limited silicon bottom cell with and without the constraint of a middle cell bandgap of $E_{g, mid} = 1.55\text{ eV}$ [18] for the triple junction structure. Without the constraint, the middle cell bandgap for detailed balance is $E_{g, mid} = 1.50\text{ eV}$. The practical potential considers further optical losses due to finite reflection and parasitic absorption losses and a maximum thickness of the perovskite absorber of 1500 nm [19, 20]. Without the constrain on the middle cell bandgap, the optimal bandgap of the practical potential is again $E_{g, mid} = 1.50\text{ eV}$. For a maximum perovskite thickness of 600 nm, the bandgap decreases to 1.45 eV. The experimental cell records of the respective structures are also shown [15, 16, 21].

30.5% to the practical potential of 44.6%, there is a gap of 14.1%_{abs} compared to the gap of 4.6%_{abs} (39.5% – 34.9%) for dual junction perovskite/silicon cells. The theoretical limit, considering Auger-limitation for the silicon bottom cell and detailed balance for the perovskite cells, is 43.2% for dual junction cells and 48.4% [18] for the triple junction cells.

One of the main challenges of two-terminal perovskite/perovskite/silicon cells is the right choice of the bandgap of the middle cell absorber. As an optimal utilization of the solar spectrum is only achieved by current matching, the appropriate bandgap combination and absorber thicknesses must be selected. Detailed balance calculations for a silicon (1.12 eV bandgap) based triple junction cell predict an ideal combination of 1.50 and 2.01 eV [17] for the perovskites. However, when considering realistic reflection and parasitic absorption, simulations indicate that the ideal bandgaps for a practical efficiency limit are around 1.45 – 1.50 eV for the middle cell and 2.00 – 2.05 eV for the top cell [20, 22], depending on the cell thicknesses. Current implementations of perovskite/perovskite/silicon cells have middle cell bandgaps ranging from 1.52 to 1.56 eV [2]. As the middle cell's bandgap is higher than optimal, current matching across all three cells is more difficult or not possible to achieve. Building a suitable and stable middle cell absorber with a bandgap between 1.45 and 1.50 eV is a relevant challenge to the field.

Perovskites within this range are available, but they typically rely on less stable Sn/Pb-based compositions [23]. FAPbI₃-based perovskites are the most promising candidates for filling this spot [24, 25] with a bandgap around 1.47 eV. However, they have degradation and phase stability issues during annealing. The cubic α -phase converts into the unfavorable polymorph δ -phase [26]. Stabilizing FAPbI₃-based perovskites is an important research topic for the perovskite-based triple junctions, as this would solve

the current matching issue. The implementation of FAPbI₃-based perovskites with a bandgap of 1.50 eV in triple junctions has also been reported [8].

For the EPFL champion cell examined in this article, a middle cell bandgap of 1.55 eV was extracted from EQE measurements. With this boundary condition of the middle cell bandgap, the maximum efficiency potential is calculated to be 46.7%. There is a difference of $\sim 5\%$ _{abs} from the dual junction to the triple structure in both the theoretical limit and the practical potential, representing the potential gain from adding a subcell to the structure. 1.6%_{abs} of this potential gain is already lost in the theoretical limit (considering Auger-limited Si) when the middle cell bandgap cannot be achieved below 1.55 eV, making surpassing the dual junction efficiency even more difficult.

This article provides guidelines for closing the gap between the current achieved efficiency and the theoretical limit by quantifying the gains from different improvements using opto-electrical numerical simulation. The simulation can resolve perovskite/perovskite/silicon triple-junction cells at the component level. It captures interface physics, individual recombination pathways, and parasitic currents. It also accounts for mobile ions and furthermore, pinpoints current and voltage losses using band-diagram analysis. These features enable a comprehensive opto-electrical loss analysis of the structure, which has not been done before. It is based on a Sentaurus TCAD [27] device simulation described in Section 2.1 and its validation is given in Section 2.2. A detailed efficiency analysis of the perovskite/perovskite/silicon cells based on device architectures developed at Fraunhofer ISE and EPFL is presented in Section 3.1.

Based on this analysis, it is evident that maximizing the short-circuit current is vital for the triple-junction cell and can be achieved by increasing the thickness of the middle perovskite

absorber to 1000–1500 nm. However, increasing the thickness may introduce additional challenges, which are further discussed in Section 3.2. Another important loss channel is recombination and transport losses in the top perovskite cell. This leads to a strong current loss at the maximum power point. The origin of this loss is identified and the critical parameters that need to be addressed are outlined in 3.3.

2 | Simulation Method

In Section 2.1, the basic models, simulated cell structures and measurement procedures are described. This paper analyzes two perovskite/perovskite/silicon triple junctions: state-of-the-art cells from Fraunhofer ISE (developed in 2024) and EPFL (developed in 2025). Hereafter, the cell from Fraunhofer ISE is referred to as “Cell A” and the cell from EPFL as “Cell B”. Cell A is described in more detail first. The differences from cell B are highlighted at the end of the section. In Section 2.2, model customization for each cell and the parameter adjustments are described.

2.1 | Modeling Approach and Simulation Input

The simulation consists of two parts. An optical simulation determines the photogeneration within each absorber. This serves as input for an electrical simulation which calculates the current-density–voltage curve (jV -curve) and band diagrams of the cell. Sentaurus TCAD [27] is used for the optical and the electrical part. The optical simulation consists of a combination of the transfer matrix method and ray-tracing. The electrical simulation is based on the drift-diffusion equation of electrons, holes, and mobile ions. Additionally, models for radiative, Shockley–Read–Hall (SRH), and Auger recombination, and tunneling are implemented. The mobile anions and cations are modeled

with a mobile charge density distribution, negative and positive, respectively. Both have the same initial density in the simulation to keep the cell electrically neutral but differ in their diffusion coefficients. The simulation has successfully modeled various solar cells in previous studies [19, 20, 28–30].

The model used in this article is based on the opto-electrical perovskite/silicon dual junction model [19], with additional customizations for the present triple junction structure (see Section 2.2). The simulation procedure for the jV -curves involves preconditioning of 500 s at open circuit and at one sun illumination, followed by reverse and forward scans performed at a scan rate of 60 mV/s. For the current density–internal voltage (iV_{OC}) curves, the average of the quasi-Fermi level splitting (divided by the elementary charge) over the absorber(s) was taken for every current.

The simulation model as well as the measurements are based on standard testing conditions, involving the AM1.5G spectrum and a temperature of 25°C [31]. Temperature changes and spectral variations in different locations around the globe can, however, significantly affect the cell performance. Triple junction can especially suffer from spectral variations as its current match situation depends on it. Bandgaps do also change with temperature. While the silicon bandgap narrows with increasing temperature, the bandgaps of perovskites enlarge [32]. It should also be noted that subcells could be driven into reverse bias, potentially destroying the device [33].

The structure of cell A [5] is shown in Figure 2a. It consists of a silicon hetero-junction (SHJ) bottom cell with a thickness of 250 μm and a textured rear side. The middle cell features PTAA as hole transport layer (HTL), a perovskite absorber with a composition of $\text{Cs}_{0.05}(\text{FA}_{0.9}\text{MA}_{0.1})_{0.95}\text{Pb}(\text{I}_{0.95}\text{Br}_{0.05})_3$ with a bandgap of $E_g = 1.56$ eV, and $\text{C}_{60}/\text{SnO}_x$ as electron transport layer (ETL)/buffer material. On top of the ITO recombination layer, the self-assembled monolayer (SAM) 2PACz is used as HTL for the $\text{Cs}_{0.20}\text{FA}_{0.71}\text{MA}_{0.09}\text{Pb}(\text{I}_{0.64}\text{Br}_{0.27}\text{Cl}_{0.09})_3$ top cell perovskite

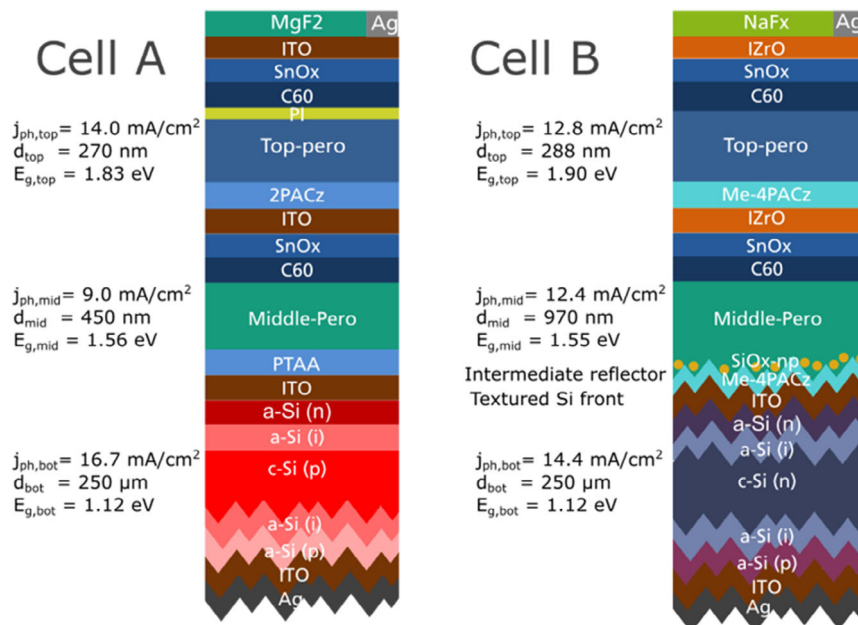


FIGURE 2 | Structure of the examined cells. The cell A on the left, and cell B on the right (adapted from [15]). The photocurrent and thickness values are based on the optical simulations, for the EQE of cell A refer to [20], for cell B to Figure S1.

absorber with a 1.83 eV bandgap. C_{60} is also used as ETL for the top cell, but with an additional piperazinium iodide (PI) passivation layer [5]. SnO_x is used as a buffer layer, ITO for recombination and lateral conduction and MgF_2 as an antireflection coating on top.

By contrast, cell B [13], which is shown in Figure 2b, uses different compositions for the middle and top perovskites, with respective bandgaps of 1.55 and 1.90 eV as determined from the measured EQE. The silicon bottom cell is an n-type rear emitter SHJ. SAM (Me-4PACz) are used for both the middle and top cells. SiO_x nanoparticles are used as a middle reflector between the middle perovskite and the silicon subcell. IZrO is used as an interconnection layer instead of ITO between perovskite subcells, and a different antireflection coating is used (NaF_x).

For the cell B, the absorber thicknesses are based on measured external quantum efficiencies and partial currents, see (Figure S1). The hole transport layers of the top and middle cells are replaced by Me-4PACz instead of 2PACz and PTAA, respectively, in the model. Their HTL interface recombination and dipole moments are adjusted according to the jV -measurements (see Section 2.2).

2.2 | Model Validation

To verify the model, it is compared against experimental data, namely the jV -curve of the individual cells and the total triple junction cell, as well as the measured iV_{OC} . This is shown in Figure 3. For cell A, the perovskite subcells are also built in the laboratory as semitransparent single junction solar cells on top of a glass substrate. They are illuminated from the same side as the triple junction solar cell. This allows the model to be adjusted individually for each subcell and then composed into a triple junction model. The thicknesses of the layers are set according to thickness measurements and an adjustment of the EQE [20]. The absorption calculated from the optical modeling is then input for the electrical simulation, in which the cell parameters were adjusted to match the shape of the jV -curve and the measured iV_{OC} .

The band parameters of the perovskites are based on ultraviolet photoelectron spectroscopy (UPS) [34] of a reference 1.68 eV perovskite with a composition of $Cs_{0.05}(FA_{0.77}MA_{0.23})_{0.95}Pb(I_{0.77}Br_{0.23})_3$. The band parameters of C_{60} (ETL) with and without PI are also taken from this reference. For the perovskites with higher or lower bandgap energy, the change in bandgap is distributed evenly to the conduction band minimum and the valence band maximum. Interface recombination, doping, and dipole moments were adjusted to match the experimental data of jV -curve and iV_{OC} measurements. Thus, the j_{sc} is mainly given by the optical input, while the V_{OC}/iV_{OC} is determined by the combination of recombination channels and band alignment of the interfaces. As the recombination currents at every channel are voltage dependent, the shape of the jV -curve and the fill-factor can be used to estimate the magnitudes of the individual channels. The hysteresis of reverse and forward scans is influenced by the ion concentration and their movement. Because of this procedure, every parameter has an uncertainty. Based on the knowledge of prior models and measurements, combined with a good agreement by parameter changes within realistic boundaries, the confidence of the model is sufficient to make some quantified statements for a loss analysis. A detailed list of the assumed parameters and jV -parameters can be found in the (Tables S1–S4).

After adjusting the model to the single junction data, it can be combined to a triple junction simulation. For cell A, however, V_{OC} is slightly underestimated and the fill factor is overestimated. This may be because a measurement procedure was used for the single junctions where it jumped to every point on the voltage axis from V_{OC} and back. This results in different ion movement and hysteresis compared to a continuous jV reverse and forward scan, which was used for the triple junction. In comparison to a single junction measurement, in the multijunction configuration, the middle cell (the current limited cell) is driven into strong reverse bias conditions, which could lead to different ion movement or potential cell damage [33].

According to the described differences of cell B in Section 2.1, the absorber thicknesses and HTL of the middle and top cell were adjusted. The current density in the actual cell is not only increased by a thicker middle cell, but also with an intermediate

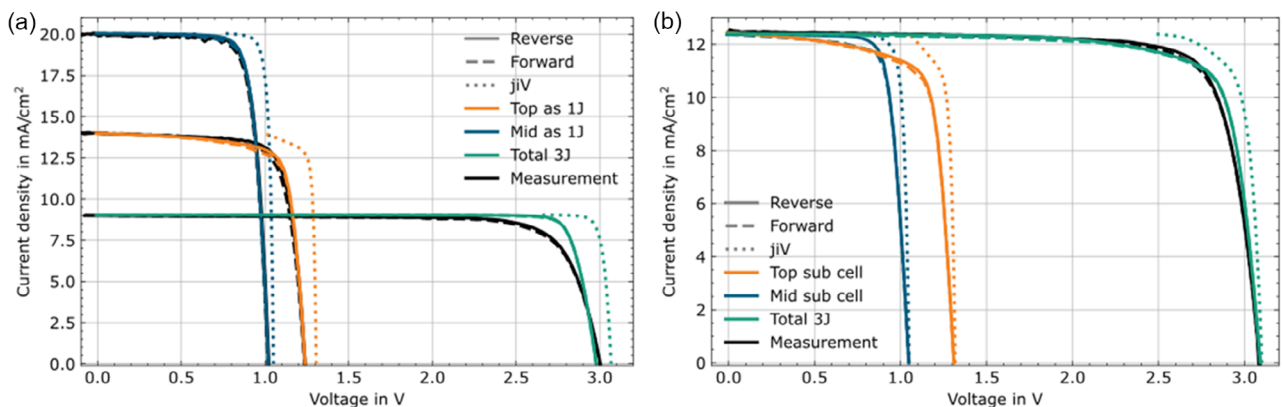


FIGURE 3 | Comparison of the simulated and measured jV -curves. The comparison with the measured data for cell A (a). Thereby, the top and middle cells are measured and simulated as single junctions, not as subcells. The reverse current-density–voltage is displayed with a solid line, the forward with a dashed line and the current-density–internal-voltage is shown dotted. Measured iV_{OC} : middle 1090 and top 1320 mV; simulated: 1050 and 1300 mV, respectively. The simulation of cell B is shown in (b), but the perovskite cells are displayed as subcells of the triple junctions, not as single junctions in this case. This is because the top single junction data is based on a different bandgap.

reflector, a front texture on the silicon and less shading caused by the metallization grid. The absorber thicknesses were adjusted to model these factors effectively. The simulation uses a thickness of 970 nm, which reflects an average of the different thicknesses caused by the texture. The single-junction jV -data from Cell B is not considered because it was built with a different bandgap than that of the subcell within the triple junction. The V_{OC} for the single junctions adds up to 3300 mV, whereas the triple junction's is 3100 mV. Adapting the model to these values would overestimate the triple junction. However, the high-performing single junctions show the high potential of the triple junction. A detailed parameter list is provided in the (Tables S1–S4).

3 | Results

This section provides a quantified electrical analysis of the examined triple junction cells. Section 3.1 analyzes both triple junction cells in terms of their loss channels. The gains of various improvements are quantified up to an electrically ideal cell. Currently, a major optical loss is the lack of current matching across all three subcells. As the middle cell bandgap is too high in perovskite/perovskite/silicon triple junction devices, the photocurrent of the middle and top perovskites will never be current matched with the silicon bottom cell. To address this, the middle perovskite can be made very thick to maximize current density for the upper two perovskite cells. However, this can lead to additional problems, as discussed in Section 3.2. Section 3.3 explains the origin of the recombination losses in the top perovskite cell, causing a strong current loss of the top cell at the maximum power point.

3.1 | Efficiency Analysis of the Perovskite/Perovskite/Silicon Structure

Based on the simulation model that was built and experimentally validated as described in Section 2, various scenarios are simulated, their impact on the cell is assessed, and the potential efficiency gains are quantified. To conduct a loss analysis, individual improvements are simulated based on the status quo (“real”) scenario, focusing on idealizing the bulk lifetime (τ), HTL, ETL, external resistance (R_{ext}), and the ion concentration (ions). Applying all these improvements then yields the “ideal” scenario. The bulk lifetime is the charge carrier lifetime within the perovskite absorber. For the transport layers, the band levels, dipole moments, doping concentration, and interface recombination are idealized. Band levels are set to be aligned with the absorbers, either by setting them in the transport layer itself or by choosing a strong enough dipole moment. Interface recombination is neglected. The external resistance represents an often-called “lumped series resistance” [35], which comprises limited conductivity on contacts or the bulk itself. It is also neglected in the ideal case. The ion concentration within each perovskite subcell describes the number of mobile ions that can lead to hysteresis effects, which is neglected in the idealized case. Anion and cation diffusivities are set based on previous studies [19]. A detailed list of the estimated real and ideal parameters can be found in the (Table S1–S4).

Cell A is initially not current-matched, which prevents a meaningful loss analysis by subcell. Therefore, the first step is to

establish current matching by adjusting the perovskite absorber thicknesses. For this, following our previous study [20], the perovskite absorber thicknesses were adjusted to 600 nm for the middle cell (from 450 nm) and to 167 nm for the top cell (from 270 nm). Thicker films are possible using state-of-the-art deposition techniques. For a complete opto-electrical roadmap, the values fit into our optical analysis [16]. The experimental Cell A is limited by the middle cell with a j_{sc} of 9.0 mA/cm² [5]. The thickness adaptation increases the triple junction current density to 11.8 mA/cm².

Starting from the current-matched baseline, each electrical improvement is applied individually to the baseline and the corresponding performance gains are summarized in Figure 4. Each scenario is applied independently to the current-matched baseline (i.e., without the other improvements). The effects of that are not strictly additive: some changes interact and produce synergistic or interfering effects [36]. To illustrate these interactions, a new analysis was performed in which all combinations of scenarios were plotted (Figure S2). This reveals the individual synergies across all involved scenarios. The analysis shows a strong synergy between HTL, ETL, and carrier lifetime (τ). This combined effect is therefore shown separately in Figure 4 as “Synergy $\tau + HTL + ETL$ ” and is discussed below.

The analysis is performed by examining the band diagrams, exemplified for cell A's middle cell in Figure S3. With an idealized ETL, the iV_{OC} increases by 35 mV due to the absence of ETL interface recombination; however, a gradient in the hole quasi-Fermi level within the perovskite bulk toward the HTL prevents efficient extraction and limits the V_{OC} gain to 10 mV. The gradient results from insufficient hole conductivity within the perovskites. This insufficiency is attributed to low hole density ($\sim 10^{10}$ cm³ at the interface) and an opposing electric field induced by ions. The gradient of the quasi-Fermi level is reflected in a difference between the internal open circuit voltage and the actual open circuit voltage, also known as selectivity loss.

Idealizing the HTL alongside reducing interface recombination introduces more holes into the absorber, enhancing hole conductivity and reducing the hole Fermi-level gradient. Selectivity losses in the middle cell are reduced from 45 to 0 mV. This improvement is magnified when combined with the ETL, as the elevated iV_{OC} can now be utilized efficiently and no selectivity losses are present. Interface recombination is suppressed at both sides, increasing the iV_{OC} and therefore the V_{OC} of the middle cell by 120 mV.

If the perovskite bulk lifetime is also improved, the iV_{OC} and thus V_{OC} are increased further. The improvement of the bulk lifetime is greater together with the transport layer enhancement because interface recombination is eliminated. This allows charge carriers that might have recombined at the interfaces to remain longer within the absorber. Thus, the bulk lifetime becomes the limiting factor, whereas interface recombination used to be the bottleneck. The combined gain from these three improvements is shown as “Synergy $\tau + HTL + ETL$ ” in red in Figure 4 in comparison to their individual gains. The middle cell of cell A can contribute an improvement of 3.2%_{abs} where synergy effects add up to 1.1%_{abs}. These mechanisms leading to the synergy effect are also true for the top cell as well as the perovskite subcells of cell B. The further scenarios are compared to the current matched scenario again, including cases with zero external

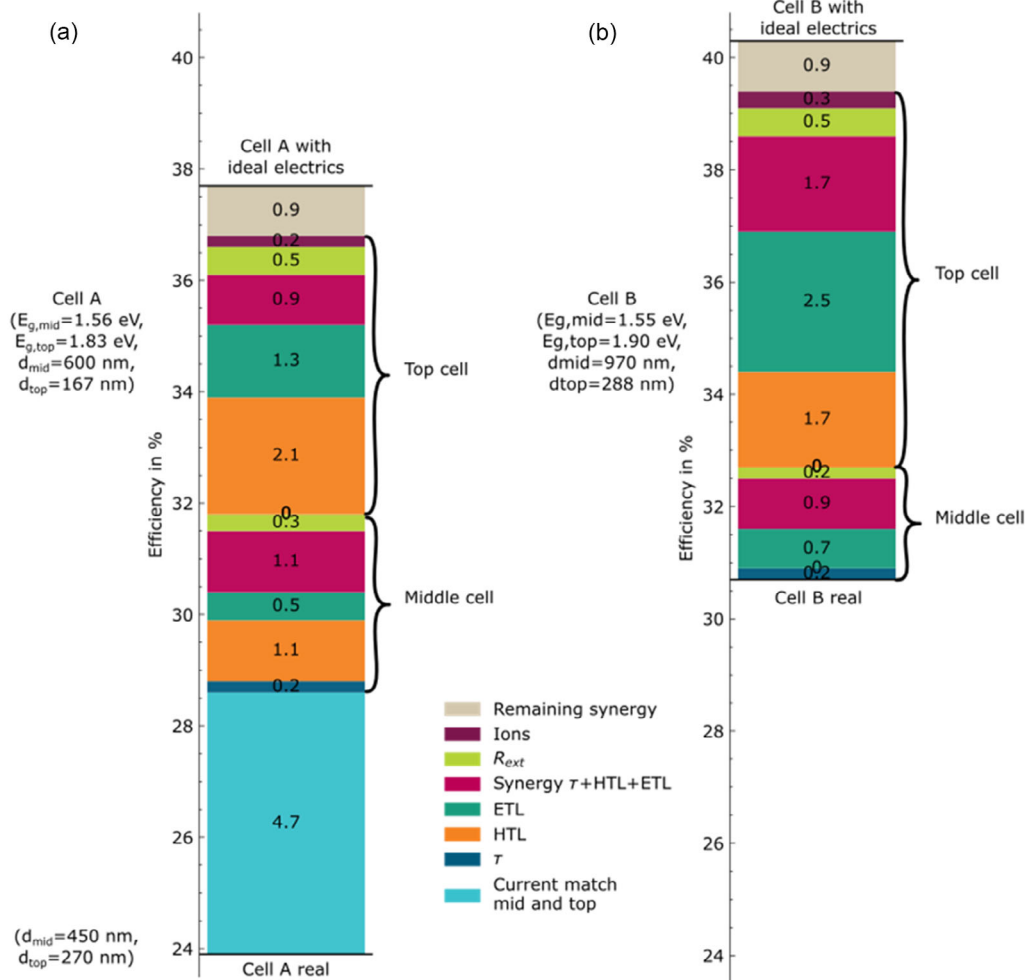


FIGURE 4 | Electrical analysis with quantified gains in absolute efficiency percentage. For cell A on the left (a), an optical adaptation is made first to get the perovskite subcells into current match. In addition, the electrical improvements are applied individually based on this scenario and the gains are quantified. The considerable synergy of combining an ideal lifetime, HTL and ETL is displayed separately. Estimations for the improvements to cell B are displayed on the right (b).

resistance in the middle cell (0.3%_{abs} gain) as well as a negligible mobile ion concentration of 10^{15} cm^{-3} (no gain). However, the loss caused by the external resistance, modeling the lumped series resistance, comprises limited conductivity on several layers and is therefore difficult to identify and provide technological advice on.

In the top cell, combining an idealized lifetime with both HTL and ETL yields an efficiency improvement of 4.3%_{abs} compared to 2.7%_{abs} for the middle cell. The loss caused by the ions in the top cell is higher (0.2%_{abs}) than in the middle cell due to an amplification of the hole recombination current discussed in Section 3.3. The “Remaining synergy” refers to the synergies between the interfaces, external resistance and ions of both perovskite cells. The ideal electrical scenario for cell A would lead to an efficiency of 37.8%.

Cell B is already well current matched between the perovskite cells, which is why a current match step is not applicable. The cell uses a SAM in the form of Me-4PACz for the middle cell instead of PTAA, resulting in a higher hole concentration at the respective interface. Therefore, the gain of idealizing the HTL in the middle cell is lower for cell B (no gain) compared to cell A (1.1%_{abs}). The HTL improvement is only apparent in combination with the ETL enhancement.

While the middle cell is closer to the electrical ideal case, there remains more potential for the top cell. This opportunity mainly arises from interface enhancements: a higher bandgap increases the theoretical open-circuit voltage, and the top cell of cell B suffers from increased hole recombination losses (see Section 3.3). Additionally, cell B exhibits a higher short-circuit current than cell A. As a result, the potential gain from improving the bulk lifetime, ETL, and HTL in the cell B’s top cell is estimated to be 5.9%_{abs} compared to the 4.3%_{abs} of the cell A’s top cell. The full electrical ideal case predicts an efficiency of 40.3% for cell B. This is 2.5%_{abs} higher than cell A, mainly due to the higher short circuit current, which stems from a thicker middle cell, and a higher top cell bandgap. However, it is 4%_{abs} below the practical potential because of the nonideal bandgaps and lower short-circuit current.

3.2 | Limitations with Fixed Bandgap of Middle Perovskite

One of the current problems of monolithic perovskite/perovskite/silicon cells is the limited current density of the middle perovskite cell. A previous study has shown the necessity of decreasing the

middle cell bandgap to around 1.45 – 1.50 eV to reach current match with the silicon bottom cell [20]. However, with an estimated bandgap of 1.55 eV and thickness of 970 nm, the photocurrent density of Cell B triple junction cell is 12.42 mA/cm² [15], compared to 14.10 mA/cm² that would be possible with a bandgap of 1.45 eV with a middle cell thickness 600 nm. Restricting the middle cell thickness to 1500 nm, the optimal bandgap would be 1.50 eV, yielding a current of 14.20 mA/cm². Therefore, if a sufficiently low bandgap cannot be achieved, the middle cell must be made thicker to improve current matching.

As cell A, on which our model is based on, has a bandgap of 1.56 eV, this is the bandgap chosen for further scenarios. We conducted optical simulations based on the boundary conditions for the bandgap of the middle perovskite absorber. A thickness variation of 400 – 1500 nm is considered for the middle cell, with the thickness of the top cell adjusted accordingly to achieve current matching between the two perovskite absorbers for each thickness, respectively. The actual thickness of the realized middle cell absorber reported reaches up to 1300 nm [4].

To illustrate the limitations of increasing the thickness of the middle cell, Figure 5 presents the *jV*-parameters for various electrical scenarios of the middle cell. Initially, ideal electrical conditions are assumed (blue) for the whole triple junction cell. Then nonideal bulk lifetime, the interfaces, the external resistance and the ion density are step-by-step included as limiting factors of the middle cell, similar to section 3.1. The effects of each scenario, as a function of the middle perovskite absorber thickness, are emphasized along with the parameters that have the most significant impact.

In the electrically ideal case (blue curves in Figure 5), the short-circuit current increases with the thickness of the middle cell. *V*_{OC} and FF slightly decrease due to the lower charge density that comes with increasing thickness.

An additional estimated bulk recombination with a SRH-lifetime of $\tau = 400$ ns, as measured in [19], is considered for the orange lines in Figure 5. Lower lifetimes lead to a lower charge density and therefore *iV*_{OC} and *V*_{OC}. A variation of bulk lifetimes is shown in Figure 6. The *V*_{OC} drops by a flat amount while the fill factor decreases for low lifetimes due to transport losses, which occur when the charge carriers recombine before they reach the interface. The primary parameter influencing the transport properties is the diffusion length *L* of the charge carriers, which is determined by both the bulk lifetime and the charge carrier mobility. Insufficient diffusion length leads to a lower maximum power point voltage, since a strong quasi-Fermi level gradient is required to extract the charge carriers. A variation of charge carrier mobility is shown in the Figure S4 for the same diffusion lengths as in Figure 6.

The next step in Figure 5 (green line) involves assuming interface conditions as chosen in the experimental validation part of Section 2.2. The ETL conduction band minimum is increased from 3.90 to 4.14 eV, and the HTL valence band maximum is decreased from 2.90 to 2.50 eV. Recombination velocity is set to 220 cm/s for the ETL and 44 cm/s for the HTL. These changes lead to a decrease in *iV*_{OC} from 3230 to 3110 mV compared to the “Lifetime” scenario for the thickest absorber of 1500 nm and an increase in the selectivity loss from 0 to 30 mV. The reduction in hole density due to the decrease of the HTL valence band maximum further intensifies the transport problem, reflected in a steeper fill factor decrease with increased cell thickness, resulting in a lower overall efficiency gain.

The next step takes an external series resistance into account (red line in Figure 5). This affects the slope of the *jV*-curve at the *V*_{OC} and reduces the fill factor by a constant amount independent of the thickness. Mobile anions and cations are then modeled with a density of $n_{\text{ions}} = 1 \cdot 10^{16}$ cm⁻³. Mobile ions introduce the hysteresis effect, which is not shown here, as only the values of the reverse

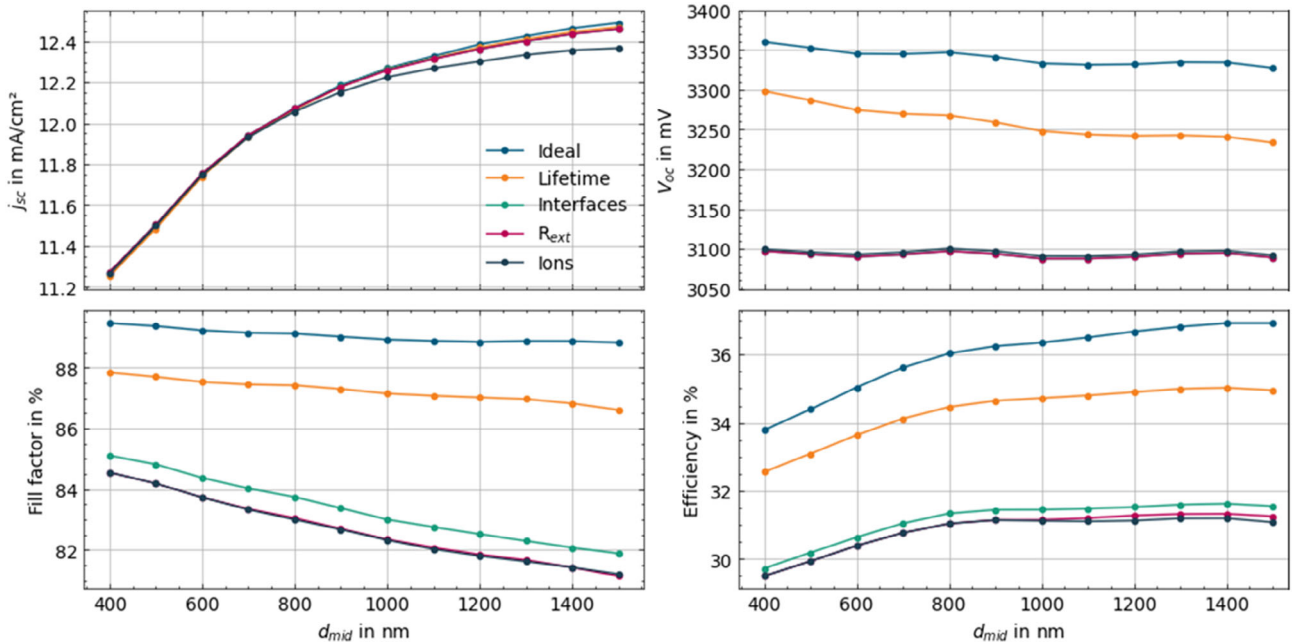


FIGURE 5 | *jV*-parameters of perovskite/perovskite/silicon cell for different scenarios. Ideal (blue) displays the practical limit. The following scenarios move toward a more realistic middle cell, while the rest of the perovskite/perovskite/silicon cell remains ideal. Lifetime (orange) adds an SRH-recombination in the bulk with $\tau = 400$ ns, interfaces (green) adds the estimated band alignment, interface recombination and dipole moment to ETL and HTL, R_{ext} (red) introduces an external resistance of $R_{\text{ext}} = 3 \Omega \text{cm}^2$, Ions (dark blue) a mobile ion density of $\rho_{\text{ion}} = 1 \cdot 10^{16} \text{cm}^{-3}$. The estimated values, and therefore the optimal thicknesses, may vary depending on the cell being viewed.

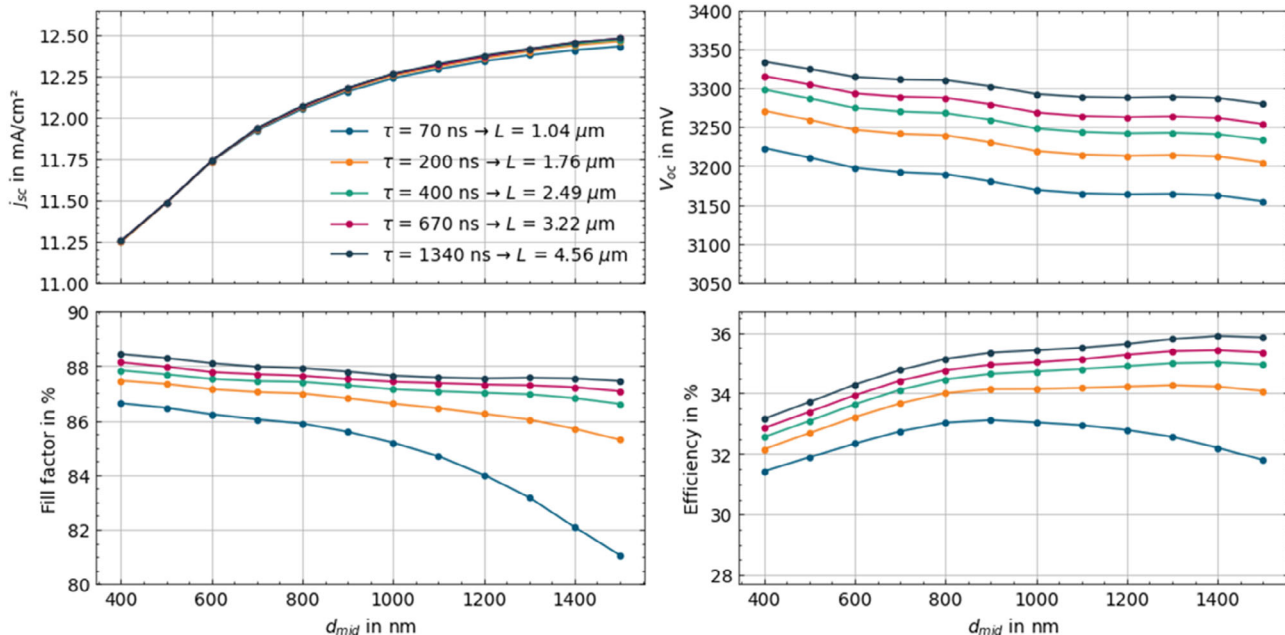


FIGURE 6 | Variation of bulk lifetimes (electrons and holes) τ for the middle cell. The estimated value of 400 ns is shown in green with a constant electron and hole mobility of 6.0 cm²/Vs. If the diffusion length L is of the same order of magnitude as the absorber thickness, great transport losses are introduced.

scans are shown. Hysteresis reduces the fill factor from reverse to forward scan. The impact of that can be seen in Figure S5.

3.3 | Recombination Losses in the Perovskite Top Cell

As mentioned in Section 3.1, a voltage-dependent current loss is observed in the perovskite top cell. Consequently, the top cell

exhibits strong current losses at the maximum power point. The reason for that could be a parasitic hole current toward the ETL contact. It is due to a low hole barrier in the valence band from the perovskite into the ETL, which can be surpassed thermally. This is shown in the band diagram of Figure 7, where the location of the parasitic hole current is marked with the gray arrow. Holes can recombine through gap states either near the interface or within the ETL bulk. In the simulation, we represent

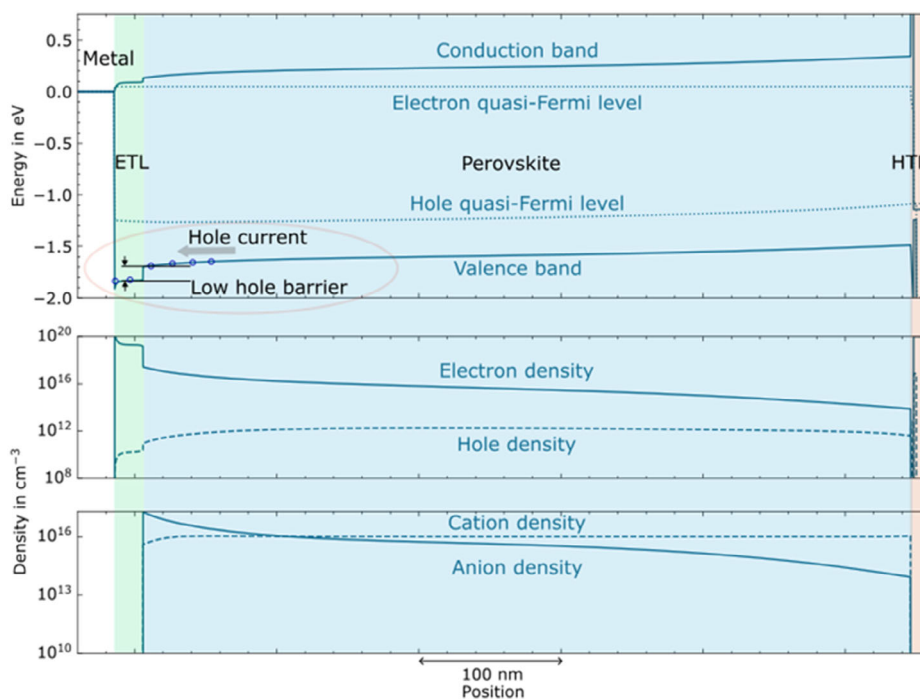


FIGURE 7 | Band diagram of the top cell of cell A at maximum power point (scenario “Real”). A parasitic hole current leads to significant current loss at maximum power point. It occurs due to a low hole barrier from the perovskite to the ETL, that can be passed thermally.

the parasitic pathway as tunneling from the perovskite into the ETL followed by recombination at the metal contact. The SnOx buffer that would block this pathway in a real device is not modeled explicitly, so this treatment serves as an effective representation of that loss mechanism.

To suppress recombination at the ETL, the valence band offset of the perovskite/ETL interface must be increased, resulting in a higher hole barrier. A variation of bandgaps of the ETL is shown in Figure 8. With a higher bandgap and constant conduction band level, the valence band is lowered, creating a hole barrier that prevents the holes from flowing to the metal contact at the ETL side. This enhances the fill factor of the top cell from 77.4% to 84.7% by increasing the ETL bandgap from 1.92 to 2.02 eV.

Another option would be to increase the hole transport toward the HTL. If the hole transport toward the HTL is improved, the amount of holes that are driven toward the ETL interface increases. The hole current j_h is given by

$$j_h = n_h \mu_h \nabla \epsilon_{FV}$$

where n_h is the hole density, μ_h the hole mobility, and $\nabla \epsilon_{FV}$ the gradient of the hole quasi-Fermi level [37]. At a given current density, if either the mobility or the hole density is too low, the gradient in the hole quasi-Fermi level compensates this, resulting in poorer transport. Conversely, the transport can be enhanced by a higher mobility or hole density. In theory, p-type doping the perovskite would also lead to the same improvement in fill factor by facilitating transport toward the HTL (see Figure S6).

The recombination losses are amplified when the perovskite's bandgap is increased. In the simulation a change in bandgap is distributed evenly to the conduction band minimum and the valence band maximum. The higher the bandgap, the lower the valence band minimum of the perovskite, the lower the hole barrier. This exemplarily shown with a band diagram for 1.80 and 2.10 eV bandgaps in Figure S7. This also explains why the recombination loss in the top cell of cell A ($E_{g, \text{top}} = 1.83$ eV) is not as pronounced as in the cell B ($E_{g, \text{top}} = 1.90$ eV).

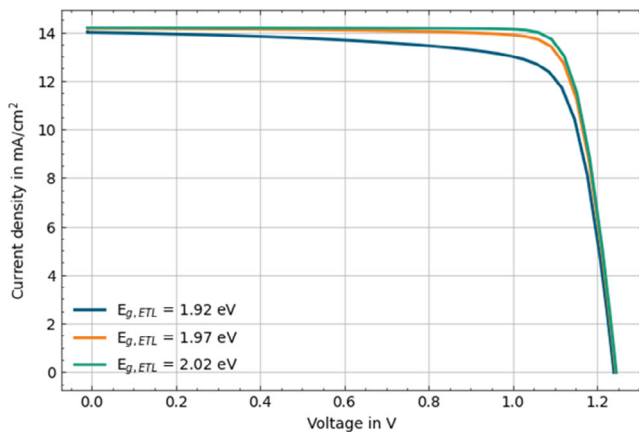


FIGURE 8 | Variation of the ETL bandgap. 1.92 eV is the bandgap chosen for C60 [34]. An increased bandgap with a fixed conduction band level leads to a lower valence band level. This creates a hole barrier from the perovskite toward the ETL to avoid a parasitic hole current toward the ETL contact.

4 | Discussion

Two state-of-the-art perovskite/perovskite/silicon triple-junction cells were modeled, and loss channels were quantified to identify the critical levers for surpassing the performance of perovskite/silicon dual-junction cells. The main barriers are the middle cell's high bandgap, which prevents current matching, and recombination losses at the top ETL.

In order to justify the process complexity of the triple junction structure, its efficiency must surpass that of the perovskite/silicon dual junction. The theoretical limit of adding a third sub-cell is 4.9%_{abs}, considering an Auger-limited silicon bottom cell. However, if the middle cell bandgap is limited to 1.55 eV due to technological constraints, the potential gain is lowered to 3.3%_{abs}, making it even more difficult to surpass the dual junction counterparts. To provide a guideline for closing the gap between the status quo and the theoretical limit, two state-of-the-art experimental cells of Fraunhofer ISE (cell A) and EPFL (cell B) were modeled, and a loss analysis was conducted using numerical device simulations.

Major improvements in electrical performance can be achieved by enhancing the extraction layers of both perovskite cells. The requirements for suitable extraction layers increase with increasing bandgap. Idealized transport layers and bulk lifetime would increase the efficiency of cell A by 2.9%_{abs} and 4.3%_{abs}, respectively, for the middle and top cell. The gains for the middle perovskite cell of cell B are smaller due to the already implemented SAM on the backside. The electrical ideal scenario predicts an efficiency of 40.3% for cell B, roughly 4%_{abs} below our estimated practical potential. This shortfall is mainly caused by a too large middle cell bandgap and incomplete surface texturing. Increasing the top cell bandgap could further raise the maximum achievable efficiency.

Achieving total current matching in the triple junction, including the bottom cell, is currently challenging due to the high middle cell bandgap. With an estimated bandgap of cell B's middle cell of 1.55 eV, the photo-current density is 12.42 mA/cm² [15]. This is lower than the 14.20 mA/cm² predicted by simulations using a 1.50 eV bandgap, 1500 nm thickness for the middle cell, and a full texture.

A straightforward approach to get closer to the current matching in the triple junction is to thicken the middle cell absorber. However, if the diffusion length, which is primarily determined by the mobility and the bulk lifetime, is of the order of the absorber size, fill factor losses will occur. High ion densities can also create an opposing field for the charge carriers, resulting in a lower short-circuit current. One way to increase the current density is to use an intermediate optical reflector below the middle cell, a feature that has already been implemented in cell B [15]. Another possible measure is the optimization of antireflection coatings [38, 39].

It was shown that the wide bandgap top cells suffer from a parasitic hole recombination current at the ETL side. This could be due to a low hole barrier from the perovskite bulk to the ETL (C_{60}). This leads to significant current losses at the maximum power point. Cell B's top cell bandgap is estimated to be 1.90 eV and the optimal top cell bandgap under the theoretical (Auger-limited) case is 2.05 eV [18]. However, the bandgap of the widely used ETL C_{60} is 1.92 eV. Thus, it does not allow

simultaneous optimal alignment with the perovskite conduction band for electron extraction and a sufficiently deep valence-band offset to block holes. If there is no hole barrier, they can recombine at gap states at the interface or in the ETL bulk. Therefore, the top cell could be improved by using an ETL with a higher bandgap (lower valence band). It is also possible to enhance hole conductivity toward the HTL in order to suppress interface recombination at the ETL. This would require a significant improvement in hole conductivity, either through increased mobility or carrier density.

The perovskite/perovskite/silicon triple junction structure has great potential to play a role in the next generation photovoltaic technology. However, the challenges of a suitable middle cell bandgap, as well as suitable transport layers, especially for high bandgap cells must be tackled. As the triple junction community can benefit from the rapid development of perovskites in general and the perovskite/silicon dual junction structure in particular, it remains a promising candidate for high-efficiency, low-cost solar cells.

Acknowledgments

This work was funded by the Deutsche Forschungsgemeinschaft (DFG) (SPP 2196: Perovskite Semiconductors: From Fundamental Properties to Devices, project number 402726906). This work was partially supported by the European Union through the Horizon Europe project (TRIUMPH) under the number 101075725 and the German Federal Ministry for Economic Affairs and Climate Action (BMWK) under contract number 03EE1132A (RIESEN).

Open Access funding enabled and organized by Projekt DEAL.

Funding

This study was supported by the Deutsche Forschungsgemeinschaft (402726906), HORIZON EUROPE Excellent Science (101075725), Bundesministerium für Wirtschaft und Energie (03EE1132A).

Conflicts of Interest

The authors declare no conflicts of interest.

Data Availability Statement

The data that support the findings of this study are available from the corresponding author upon reasonable request.

References

1. J. Werner, F. Sahli, F. Fu, et al., “Perovskite/Perovskite/Silicon Monolithic Triple-Junction Solar Cells with a Fully Textured Design,” *ACS Energy Letters* 3, no. 9 (2018): 2052–2058.
2. M. Heydarian, M. Heydarian, P. Schygulla, et al., “Recent Progress in Monolithic Two-Terminal Perovskite-Based Triple-Junction Solar Cells,” *Energy & Environmental Science* 17, no. 5 (2024): 1781–1818, <https://pubs.rsc.org/en/content/articlelanding/2024/ee/d3ee02822d>.
3. F. Li, D. Wu, Le Shang, et al., “Highly Efficient Monolithic Perovskite/Perovskite/Silicon Triple-Junction Solar Cells,” *Advanced Materials* 36, no. 16 (2024): e2311595, <https://advanced.onlinelibrary.wiley.com/doi/10.1002/adma.202311595>.
4. S. Liu, Y. Lu, C. Yu, et al., “Triple-Junction Solar Cells with Cyanate in Ultrawide-Bandgap Perovskites,” *Nature* 628, no. 8007 (2024): 306–312, <https://www.nature.com/articles/s41586-024-07226-1>.
5. M. Heydarian, A. Shaji, O. Fischer, et al., “Minimizing Open-Circuit Voltage Losses in Perovskite/Perovskite/Silicon Triple-Junction Solar

Cell with Optimized Top Cell,” *Solar RRL* 9, no. 3 (2025): 2400645, <https://onlinelibrary.wiley.com/doi/full/10.1002/solr.202400645>.

6. Y. Gupta, M. Heydarian, M. Heydarian, et al., “Photostable Inorganic Perovskite Absorber via Thermal Evaporation for Monolithic Perovskite/Perovskite/Silicon Triple-Junction Solar Cells,” *Progress in Photovoltaics* 33, no. 7 (2025): 782–794, <https://onlinelibrary.wiley.com/doi/10.1002/pip.3923>.
7. F. Xu, E. Aydin, J. Liu, et al., “Monolithic Perovskite/Perovskite/Silicon Triple-Junction Solar Cells with Cation Double Displacement enabled 2.0 eV Perovskites,” *Joule* 8, no. 1 (2024): 224–240, <https://www.sciencedirect.com/science/article/pii/S2542435123004920>.
8. F. Xu, E. Aydin, I. Yavuz, et al., “Stabilized Perovskite Phases Enabling Efficient Perovskite/Perovskite/Silicon Triple-Junction Solar Cells,” *Nature Materials* 2025: 1.
9. J. Zheng, G. Wang, L. Duan, et al., “Tailoring Nanoscale Interfaces for Perovskite-Perovskite-Silicon Triple-Junction Solar Cells,” *Nature Nanotechnology* 20, no. 11 (2025): 1648–1655.
10. M. Heydarian, M. Heydarian, A. J. Bett, et al., “Monolithic Two-Terminal Perovskite/Perovskite/Silicon Triple-Junction Solar Cells with Open Circuit Voltage 2.8 V,” *ACS Energy Letters* 8, no. 10 (2023): 4186–4192.
11. H. Hu, S. X. An, Y. Li, et al., “Triple-Junction Perovskite-Perovskite-Silicon Solar Cells with Power Conversion Efficiency of 24.4,” *Energy and Environmental Science* 17, no. 8 (2024): 2800–2814, <https://pubs.rsc.org/sw/content/articlelanding/2024/ee/d3ee03687a>.
12. J. Zheng, G. Wang, W. Duan, et al., “Monolithic Perovskite-Perovskite-Silicon Triple-Junction Tandem Solar Cell with an Efficiency of over 20%,” *ACS Energy Letters* 7, no. 9 (2022): 3003–3005.
13. T. Ye, L. Qiao, T. Wang, et al., “Molecular Synergistic Effect for High Efficiency Monolithic Perovskite/Perovskite/Silicon Triple-Junction Tandem Solar Cells,” *Advanced Energy Materials* 14, no. 44 (2024): 2402491, <https://advanced.onlinelibrary.wiley.com/doi/10.1002/aenm.202402491>.
14. ACS Publications, “Rational Design of Medium-Bandgap Perovskite Solar Cells for Triple-Junction Si Tandems,” Accessed August 22, 2025, <https://pubs.acs.org/doi/full/10.1021/acsami.4c22601>.
15. K. Artuk, D. Turkay, A. G. Kuba, et al., “Perovskite-Perovskite-Silicon Triple Junction Solar Cells with Improved Carrier and Photon Management,” 2025, <https://www.researchsquare.com/article/rs-7077073/v1>.
16. LONGi Breaks World Record for Crystalline Silicon-Perovskite Tandem Solar Cell Efficiency Again -LONGi, accessed July 15, 2025, <https://www.longi.com/en/news/silicon-perovskite-tandem-solar-cells-new-world-efficiency/>.
17. P. Schygulla, R. Müller, D. Lackner, et al., “Two-Terminal III-V//Si Triple-Junction Solar Cell with Power Conversion Efficiency of 35.9% at AM1.5g,” *Progress in Photovoltaics* 30, no. 8 (2022): 869–879, <https://onlinelibrary.wiley.com/doi/full/10.1002/pip.3503>.
18. A. Fell, O. Fischer, M. Bivour, et al., “Elucidating the Efficiency Limit of Silicon-Based Monolithic Tandem Cells through the Combination of Auger and Shockley-Queisser Limits,” *Royal Society of Chemistry* 1, no. 9 (2025): 1030–1039.
19. O. Er-raji, C. Messmer, A. J. Bett, et al., “Loss Analysis of Fully-Textured Perovskite Silicon Tandem Solar Cells: Characterization Methods and Simulation toward the Practical Efficiency Potential,” *Solar RRL* 7, no. 24 (2023): 2300659.
20. L. Restat, C. Messmer, M. Heydarian, et al., “Opto-Electrical Modelling of Perovskite/Perovskite/Silicon Triple-Junction Solar Cells: Towards the Practical Efficiency Potential,” *Solar RRL* 8 (2024): 2300887.
21. 2781% LONGi Refreshes the World Record for the Efficiency of Monocrystalline Silicon Cells Again -LONGi, Accessed July 22, 2025, <https://www.longi.com/en/news/isfh-hbc-conversion-efficiency/>.

22. M. T. Hörantner, T. Leijtens, M. E. Ziffer, et al., "The Potential of Multijunction Perovskite Solar Cells," *ACS Energy Letters* 2, no. 10 (2017): 2506–2513.
23. H. Hu, S. Moghadamzadeh, R. Azmi, et al., "Sn-Pb Mixed Perovskites with Fullerene-Derivative Interlayers for Efficient Four-Terminal All-Perovskite Tandem Solar Cells," *Advanced Functional Materials* 32, no. 12 (2022): 2107650, <https://advanced.onlinelibrary.wiley.com/doi/full/10.1002/adfm.202107650>.
24. G. E. Eperon, S. D. Stranks, C. Menelaou, M. B. Johnston, L. M. Herz, and H. J. Snaith, "Formamidinium Lead Trihalide: A Broadly Tunable Perovskite for Efficient Planar Heterojunction Solar Cells," *Energy and Environmental Science* 7, no. 3 (2014): 982, <https://pubs.rsc.org/en/content/articlelanding/2014/ee/c3ee43822h>.
25. H. Chen, Y. Chen, T. Zhang, X. Liu, X. Wang, and Y. Zhao, "Advances to High-Performance Black-Phase FAPbI₃ Perovskite for Efficient and Stable Photovoltaics," *Small Structures* 2, no. 5 (2021): 2000130, <https://onlinelibrary.wiley.com/doi/10.1002/ssr.202000130>.
26. Z. Zheng, S. Wang, Y. Hu, Y. Rong, A. Mei, and H. Han, "Development of Formamidinium Lead Iodide-Based Perovskite Solar Cells: Efficiency and Stability," *Chemical Science* 13, no. 8 (2022): 2167–2183, <https://pubs.rsc.org/en/content/articlelanding/2022/sc/d1sc04769h>.
27. Synopsys | EDA Tools, "Semiconductor IP and Application Security Solutions," Accessed June 27, 2023, <https://www.synopsys.com/>.
28. C. Messmer, M. Bivour, J. Schon, S. W. Glunz, and M. Hermle, "Numerical Simulation of Silicon Heterojunction Solar Cells Featuring Metal Oxides as Carrier-Selective Contacts," *IEEE Journal of Photovoltaics* 8, no. 2 (2018): 456–464.
29. C. Messmer, D. Chojniak, A. J. Bett, et al., "Towards More Reliable Measurement Procedures of Perovskite-Silicon Tandem Solar Cells: The Role of Transient Device Effects and Measurement Conditions," *Progress in Photovoltaics: Research and Applications* 33 (2023): 126.
30. M. Heydarian, C. Messmer, A. J. Bett, et al., "Maximizing Current Density in Monolithic Perovskite Silicon Tandem Solar Cells," *Solar RRL* 7, no. 7 (2023): 2200930, <https://onlinelibrary.wiley.com/doi/full/10.1002/solr.202200930>.
31. Reference Air Mass 1.5 Spectra | Grid Modernization | NREL, accessed November 27, 2025, <https://www.nrel.gov/grid/solar-resource/spectra-am1.5>.
32. G. Mannino, I. Deretzis, E. Smecca, et al., "Temperature-Dependent Optical Band Gap in CsPbBr₃, MAPbBr₃, and FAPbBr₃ Single Crystals," *Journal of Physical Chemistry Letters* 11, no. 7 (2020): 2490–2496.
33. M. Heydarian, A. J. Bett, C. Messmer, et al., "Impact of Perovskite Subcell Breakdown on the Performance of Perovskite/Perovskite/Silicon Triple-Junction Solar Cells," *Solar RRL* 8, no. 16 (2024): 2400376, <https://onlinelibrary.wiley.com/doi/full/10.1002/solr.202400376>.
34. S. Mariotti, E. Köhnen, F. Scheler, et al., "Interface Engineering for High-Performance, Triple-Halide Perovskite-silicon Tandem Solar Cells," *American Association for the Advancement of Science* 381 (July 2023): 63, <https://www.science.org/doi/10.1126/science.adf5872#sec-6>.
35. O. Fischer, A. J. Bett, Y. Zhu, et al., "Revealing Charge Carrier Transport and Selectivity Losses in Perovskite Silicon Tandem Solar Cells," *Matter* 8, no. 12 (2025): 102404, [https://www.cell.com/matter/fulltext/S2590-2385\(25\)00447-3](https://www.cell.com/matter/fulltext/S2590-2385(25)00447-3).
36. J. H. Petermann, Prozessentwicklung & Verlustanalysen für dünne Monokristalline Siliziumsolarzellen Und Deren Prozessierung Auf Modullevel (Gottfried Wilhelm Leibniz Universität Hannover, 2014).
37. U. Würfel, A. Cuevas, and P. Würfel, "Charge Carrier Separation in Solar Cells," *IEEE Journal of Photovoltaics* 5, no. 1 (2015): 461–469.
38. M. Moayedfar and M. K. Assadi, "Various Types of Anti-Reflective Coatings (Arcs) Based on the Layer Composition and Surface Topography: A Review," *Reviews on Advanced Materials Science* 53, no. 2 (2018): 187–205, <https://www.degruyter.com/document/doi/10.1515/rams-2018-0013/html>.
39. H. K. Raut, V. A. Ganesh, A. S. Nair, and S. Ramakrishna, "Anti-Reflective Coatings: A Critical, in-Depth Review," *Energy and Environmental Science* 4, no. 10 (2011): 3779, <https://pubs.rsc.org/en/content/articlehtml/2011/ee/c1ee01297e>.

Supporting Information

Additional supporting information can be found online in the Supporting Information section. **Supporting Fig. S1:** EQE of the EPFL cell (Cell B). The thicknesses and bandgaps are adjusted to match the measured shape and current density. The current density of the Silicon cell is underestimated, but this does not change the 3J performance because the current density in the silicon sub cell is higher than in the perovskite cells. The EQE of the silicon subcell would be better represented if it was averaged over different middle cell thicknesses, as the front side of the Silicon is textured. **Supporting Fig. S2:** Individual losses for all possible scenarios for the top (a) and middle (b) subcells of cell B. The real scenario is displayed on the left, while from left to right the scenarios τ , HTL, ETL, R_{ext} , Ions are idealized. The thickness of a connection line displays the gain of adding an idealization. The scenarios, HTL, ETL have a strong synergy effect while R_{ext} , Ions are less correlated. **Supporting Fig. S3:** Band diagram of cell A at maximum power point in the "current match" scenario, i.e. the upper two perovskite cells are current matched, but the electrical parameters are the same as in the "real" cell and not idealized yet. The difference of the internal voltage and the outer voltage is caused by the gradient in the hole quasi-Fermi level, marked in red. **Supporting Fig. S4:** Variation of the mobility of the middle cell with a constant lifetime of 400 ns. **Supporting Fig. S5:** Reverse and forward scan with an ion density of 10^{16} cm^{-3} . **Supporting Fig. S6:** Variation of positive doping. Increased positive doping leads to better hole conductivity and therefore prevents the hole from tunnel into the ETL. **Supporting Fig. S7:** Band diagram and jV-curve for different top cell bandgaps at maximum power point. The top cell of cell B is simulated with different bandgaps but the same illumination profiles. The change in bandgap is distributed evenly to valence and conduction band. The higher the perovskite top cell bandgap, the greater the hole recombination loss. **Supporting Table S1:** Electrical simulation parameters. **Supporting Table S2:** Cell thicknesses. **Supporting Table S3:** Absorber bandgaps. **Supporting Table S4:** jV parameters of cell A.